Modeling of the Lower Ionosphere during Solar *X*-ray Flares of Different Classes

S. Z. Bekker[1,2] and I. A. Ryakhovsky[1]

[1] Sadovsky Institute of Geospheres Dynamics, Russian Academy of Sciences, Moscow, Russia.

[2] Moscow Institute of Physics and Technology, Moscow, Russia.

Corresponding author: Susanna Bekker (susanna.bekker@gmail.com)

Key Points:

- A plasma-chemical model of the ionospheric *D*-region is presented
- Model allows to predict ionosphere parameters behavior during *C*- and *M*-class flares with sufficient accuracy
- Verification of the obtained results was carried out with use of ground-based radiophysical measurements

Abstract

This paper presents the results of modeling the lower ionosphere response to solar *X*-ray flares of *C*-, *M*- and *X*-classes. The model is based on a 5-component scheme of the ionization-recombination cycle of the ionospheric *D*-region. Input parameters of the plasma-chemical model under different heliogeophysical conditions corresponding to selected *X*-ray flares were determined by using data received from AURA, SDO and GOES satellites. Verification of the obtained results was carried out with use of ground-based radiophysical measurements taken at the geophysical observatory Mikhnevo. Results of comparing the calculated and experimental the radio wave amplitude variations along six European very low frequency (VLF) paths show that the root mean square error (RMSE) does not exceed 1.5 dB for ~70% of cases including *X*-class flares during which the amplitude jump on some paths reaches 8 dB. Qualitative and quantitative analysis of the verification results of the VLF signal amplitude has showed the good predictive capability of the built model for describing weak and moderate ionospheric disturbances.

1 Introduction

At present, researchers intensively develop modeling of all layers of ionosphere for solving research problems of various profiles, as well as for applied tasks, in particular, improvement of the estimates' accuracy of propagation of radio waves in a wide range of frequencies.

Despite the fact that now there is a significant number of theoretical estimates and experimental data on the processes occurring in ionospheric plasma and about the spatial and temporal distribution of concentrations of its components (Bilitza et al., 2017; Marsh et al., 2013; Nava et al., 2008; Wait & Spies, 1964), the prediction accuracy of ionospheric parameters, especially under conditions of various disturbances, is low.

The lower part of the ionosphere (h ~ 60–90 km) remains the least studied by now. Difficulties in studying the *D*-region is due to a large number of photochemical processes and incapability of continuous measuring the ionosphere parameters, first of all, concentration of electrons *Ne*, at these amplitudes (Egorova et al., 2011; Friedrich et al., 2018; Krivolutsky et al., 2015; Turunen et al., 1992, 1996; Verronen et al., 2005, 2016).

State of the lower ionosphere parameters is determined by the latitude and space weather factors, such as solar cosmic rays, magnetospheric storms, precipitation of charged particles, ionizing electromagnetic radiation (Kumar et al., 2015, 2017; Kumar & Kumar, 2018; Maurya et al., 2012, 2018; Peter et al., 2006; Thomson et al., 2004, 2005). Solar flares are accompanied by considerably increased intensity of *X*-radiation, which leads to a significant change of the electron concentration in the illuminated area of the lower ionosphere (Grubor et al., 2005, 2008; Mitra, 1974; Nina et al., 2011; Poppoff & Whitten, 1962; Ryakhovskiy et al., 2018). Such *Ne* variations significantly distort the amplitude and phase characteristics of the very low frequency (VLF) signals within a range 3–30 kHz propagating in the Earth-ionosphere waveguide with the *D*-region as its upper boundary (Brunelli & Namgaladze, 1988; Gavrilov et al., 2019a; Han et al., 2011; Hargreaves, 1995; Schunk & Nagy, 2009; Wait & Spies, 1964). This allows using the measurements of amplitude and phase of VLF signals for studying the state of lower ionosphere, and applying them as a tool for verification of the medium models (Bekker et al., 2018; Lyakhov et al., 2018; Palit et al., 2013). Verification on the basis of data of ground-based radiophysical

measurements allows the direct assessment of the model's predictive capability at solving problems of the VLF signal propagation. Moreover, the quantity of radiophysical data is many orders of magnitude greater than the electron concentration measurements taken for the *D*-region, which makes it possible to carry out verification under almost any heliogeophysical conditions including the solar flares.

This work is devoted to modeling the lower ionosphere during solar *X*-ray flares of different classes and analysis of the results obtained by verification with the ground-based radiophysical measurements taken at the Mikhnevo geophysical observatory of Sadovsky Institute of Geospheres Dynamics (Gavrilov et al., 2017, 2019a).

2 Experimental data obtained at the Mikhnevo Geophysical Observatory

Since 2014, Mikhnevo has been continuously monitoring the amplitude and phase characteristics of electromagnetic signals from the VLF transmitters located throughout the world (Gavrilov et al., 2019b).

To verify the results of the modeling we used measurements of the amplitude of the signals received at the Moscow region observatory Mikhnevo (55°N 38°E) from six transmitters located at the European midlatitudes (Figure 1). The main characteristics of the transmitters are listed in Table 1.

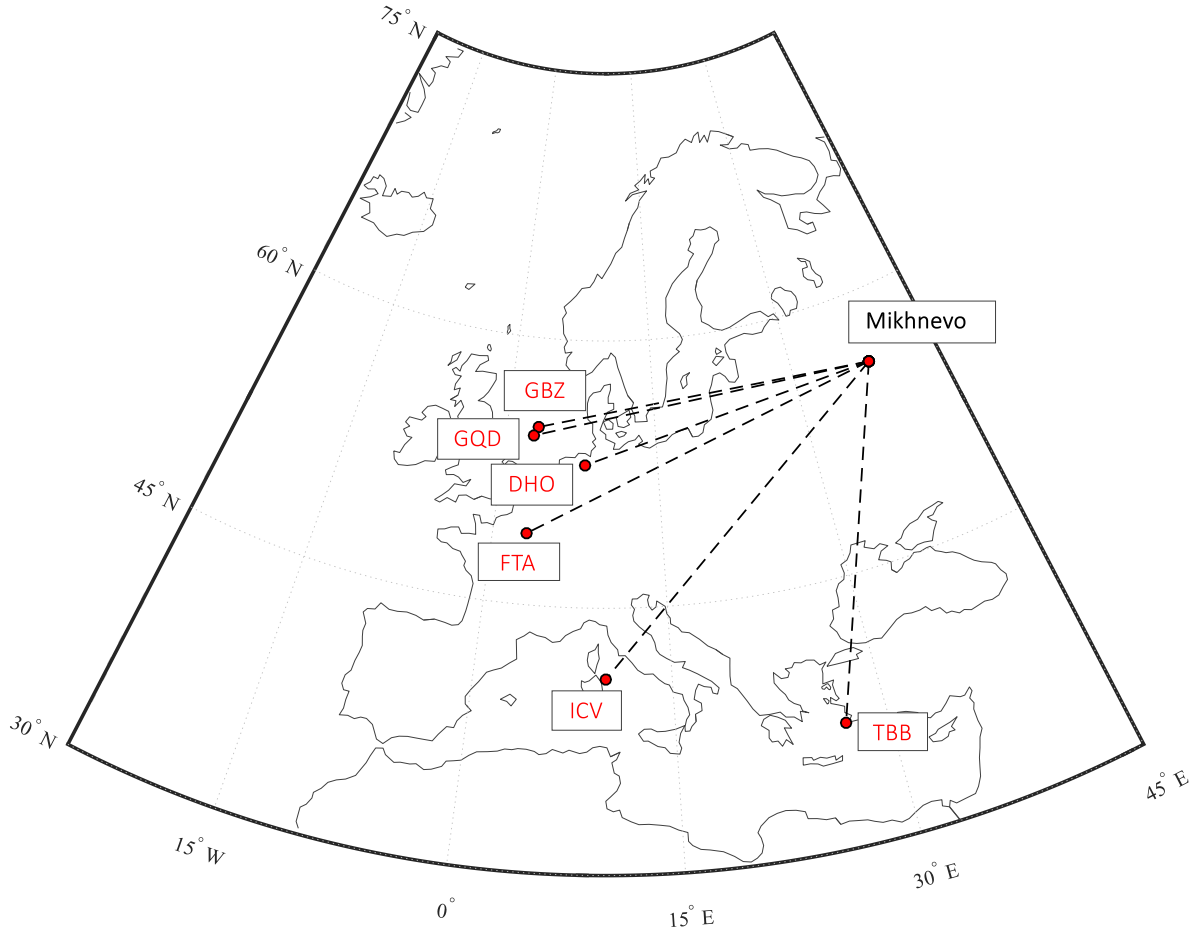

Figure 1. The locations of the Mikhnevo geophysical observatory and the VLF transmitters.

Table 1

Main Characteristics of the VLF Signal Transmitters

Station	Location	Coordinates	Frequency [kHz]	Path length [km]
GBZ	England	55°N 3°W	19.6	2585
ICV	Italy	41°N 10°E	20.3	2580
FTA	France	49°N 3°E	20.9	2500
GQD	England	55°N 3°W	22.1	2565
DHO	Germany	53°N 8°E	23.4	1960
TBB	Turkey	37°N 27°E	26.7	2100

The amplitude of the signal passing through the simulated medium was calculated by using the LWPC program (Ferguson, 1998). The configured nominal power of the transmitters was 1 kW. Amplitude values were taken in [dB] for the purpose of quantitative comparison of theoretical and experimental daily variations. The amplitude shift due to the difference between the unknown actual transmitter power and the one used for the calculations was determined by the difference of the theoretical amplitude value and the experimental data obtained at a quite heliogeophysical day that preceded each considered flare (Palit et al., 2013).

3 Plasma-chemical model of the lower ionosphere

As stated in the introduction, at present there are a significant number of empirical and theoretical models of the lower ionosphere, describing its state with some accuracy. For solving applied problems of the radio wave propagation, the two-parameter Wait-Ferguson model (Ferguson, 1995; Wait & Spies, 1964) is most often used. On the one hand, this model makes it possible to simulate the radioequivalent ionosphere to successfully use its results for calculating the radio wave propagation. On the other hand, the modeled vertical electron concentration profiles can be not corresponding to the real ones, since the model is based on the exponential *Ne* profile.

When choosing the number of plasma-chemical processes on which the model under development is based, it is necessary to take into account not only the expected accuracy of the results, but also the possibility of rapid calculation of the environmental parameter variations at natural disturbances. Today, there are global three-dimensional numerical models of the lower ionosphere, taking into account hundreds and thousands of known photochemical reactions. These models describe the behavior of ionospheric components under the calm conditions and under the influence of various disturbances (Krivolutsky et al., 2015; Turunen et al., 1992, 1996; Verronen et al., 2016). However, such models require extremely high computational power and time resources, and therefore, the applied tasks of forecasting radio wave propagation cannot be promptly solved with it. Moreover, the number of unknown reaction rate constants increases with the number of considered plasma-chemical processes, which can lead to higher errors.

The system of differential equations of the ionization-recombination cycle describes the behavior of charged and neutral components, the dynamics of which are most important at *D*-region heights. Analysis of the results of calculating the electron concentration in the 4-component (Glukhov et al., 1992), 5-component (Egoshin et al., 2012) and 8-component (Kudryavtsev and Romanyukha, 1995) plasma-chemical models of the lower ionosphere has

showed no significant difference between the results of the two latter. However, not accounting the variations of concentration of the negative cluster ions, absent in the 4-component model, leads to a noticeable decrease of the *Ne* concentration at altitudes less than 70 km, which fundamentally affects the results of calculation of the VLF radio wave propagation both under the calm conditions and at *X*-ray flares.

Therefore, the 5-component ionization-recombination cycle of the ionospheric *D*-region (1) has been selected for this work as the most optimal. The system describes the behavior of concentration of electrons *Ne* and 4 ion types: NO^+, O_2^-, positive and negative cluster ions XY^+, XY^-. It takes into account almost all major photochemical processes occurring in the lower ionosphere.

$$
\begin{cases}
\dfrac{d[NO^+]}{dt} = q - 4\cdot10^{-7}\left(\dfrac{300}{T}\right)^{1/5}[NO^+]N_e - B[NO^+] - 10^{-7}[NO^+]\left([O_2^-]+[XY^-]\right); \\
\dfrac{d[XY^+]}{dt} = B[NO^+] - 2.55\cdot10^{-5}[XY^+]N_e - 10^{-7}[XY^+]\left([O_2^-]+[XY^-]\right); \\
\dfrac{d[O_2^-]}{dt} = 1.4\cdot10^{-29}\left(\dfrac{300}{T}\right)\exp\left(-\dfrac{600}{T}\right)[O_2]^2 N_e - 0.33[O_2^-] - 4\cdot10^{-10}[O_3][O_2^-] - \\
-10^{-7}[O_2^-]\left([NO^+]+[XY^+]\right) - 4\cdot10^{-31}[O_2]^2[O_2^-]; \\
\dfrac{d[XY^-]}{dt} = 4\cdot10^{-10}[O_3][O_2^-] + 4\cdot10^{-31}[O_2]^2[O_2^-] - 10^{-7}[XY^-]\left([NO^+]+[XY^+]\right) - [XY^-]; \\
\dfrac{dN_e}{dt} = \dfrac{d[NO^+]}{dt} + \dfrac{d[XY^+]}{dt} - \dfrac{d[O_2^-]}{dt} - \dfrac{d[XY^-]}{dt}; \\
B = 1.8\cdot10^{-28}\left(308/T\right)^{4.7}[H_2O][N_2] + \dfrac{2\cdot10^{-31}\left(300/T\right)^{4.4}[N_2]^2\times10^{-9}[H_2O]}{C} + \\
+\dfrac{10^{-9}[H_2O]}{3.1\cdot10^4 T^{-4}\exp\left(-4590/T\right)[N_2]+10^{-9}[H_2O]}\times \\
\times\left(7\cdot10^{-30}\left(300/T\right)^3[CO_2][N_2] + \dfrac{2\cdot10^{-31}\left(300/T\right)^{4.4}[N_2]^2\times10^{-9}[CO_2]}{C}\right); \\
C = 1.5\cdot10^6 T^{-5.4}\exp\left(-2450/T\right)[N_2]+10^{-9}\left([CO_2]+[H_2O]\right).
\end{cases}
\tag{1}
$$

3.1 Input data

The system input parameters are the ionization rate *q*, concentration of neutrals *M*, temperature *T*, and concentration of small neutral components [H_2O], [CO_2], [O_3].

It is known that ionization rate is the key parameter responsible for change of the *Ne* concentration during solar flares, that is why its calculation must be particularly careful. At the same time, for a correct modeling of the lower ionosphere during disturbances of various nature, we need to know the state of the medium before and after the perturbation, in other words we must correctly calculate the background *Ne* values. There are at least two reasons for this. First, the accuracy of calculating the background concentration of *Ne* significantly affects the quality of modeling small solar flares (Palit et al., 2013). Second, vertical profiles of *Ne* during the calm

Sun are used to normalize the radio wave amplitude during verification of the results (see paragraph 2). At the same time, the accuracy of calculation of background electron concentration values in addition to the ionization rate significantly depends on the temperature and concentration of neutrals (Bekker, 2018). Therefore, a great attention was paid to the accuracy of determining not only q, but also other parameters of the system (1).

In order to obtain the most reliable values of T, $[N_2]$, $[O_2]$, $[H_2O]$ and $[O_3]$, a statistical analysis of the experimental atmospheric data obtained by the AURA satellite from 2004 to 2018 (Livesey et al., 2013) was performed.

It is obvious that at solving the system of ionization-recombination cycle under some specific heliogeophysical conditions, use of averaged values rather than separate measurements from satellite as input parameters seems to be more correct. Besides, it is necessary to approach such averaging carefully, because the results of calculation of the electron concentration significantly depend on the selected ranges of the heliogeophysical conditions - latitude, longitude, zenith angle, season, index $F10.7$. On the one hand, the selected ranges of heliogeophysical conditions should be wide enough to include a representative sample of measurements, and on the other hand, a considered parameter should not change significantly within the given limits. To solve this problem, the daily, seasonal, latitudinal, and longitudinal dependences of satellite data T, $[N_2]$, $[O_2]$, $[H_2O]$, and $[O_3]$, as well as the dependence on solar activity, were considered. For each of the parameters, the probability density functions were built and their dynamics were analyzed when each heliogeophysical condition changed in its turn with the other conditions fixed.

Figure 2 shows the neutrals temperature T dependence on latitude for different months at an altitude of h = 60 km. The colors in the figure correspond to the values of the probability density function of temperature $P(T)$ normalized to its maximum. As can be seen, the temperature has the latitudinal dependence, therefore, the latitude step $\Delta\varphi$ must be selected in such a way that the temperature does not change significantly. For example, during the summer months, when choosing $\Delta\varphi = 10°$ the difference between the nearby latitudinal T values does not exceed 3.5%.

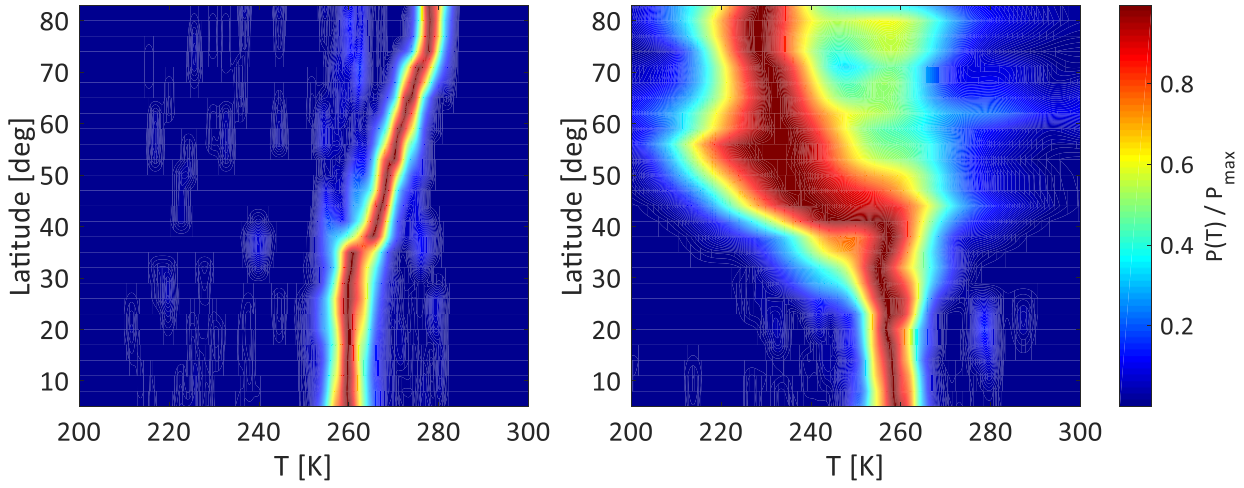

Figure 2. Dependence of the normalized probability density function $P(T)$ on latitude based on (left panel) the June data and (right panel) the December data (h = 60 km).

Besides, one should pay attention to how the function $P(T)$ varies with a season. Not only does the average value profile differ, but also its dispersion; the spread of values for the winter period is much larger than that of summer. This point was also taken into account for the simulation and temperature values were considered for each month separately.

The analysis of behavior of $P(T)$ function at various sets of heliogeophysical conditions has showed that temperature has a clear dependence on season and latitude within the considered altitude range and at any level of solar activity.

The next parameter essentially influencing *Ne* at the *D*-region altitudes is concentration of neutrals *M*. It is found that the average concentration does not depend on latitude, however the increased spread of values is clearly observed at approach to the poles. The seasonal value change is seen only at $h \leq 80$ km and not for the entire range of latitudes. Figure 3 shows the seasonal variation of neutrals concentration *M* for different latitude ranges at an altitude of 75 km. The colors in the figure correspond to the values of the probability density function $P(M)$ normalized to its maximum. As follows from the Figure 3, the seasonal *M* profile is seen at latitudes $\varphi > 40°$, and within the equatorial part, its value is almost constant. Since the concentration at low latitudes does not depend on the season, it is natural that the dispersion of concentrations here is lesser.

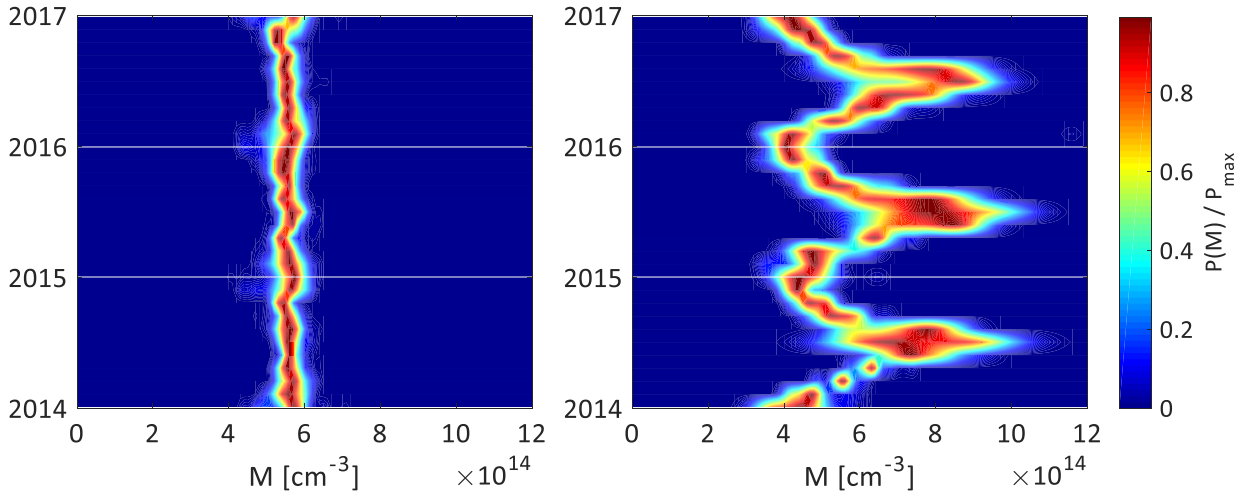

Figure 3. The seasonal dependence of the normalized probability density function $P(M)$ for (left panel) $0° < \varphi < 40°$ and (right panel) $\varphi > 40°$ (h = 75 km).

The daily variations of temperature and concentration of neutrals is not detected at any of the altitudes. As for solar activity; as a rule, the dispersion of values increases with its growth, but the median remains practically unchanged.

The behavior of small neutral components is nearly the same as that of the concentration of neutrals *M*, since experimental satellite measurements of $[H_2O]$, $[O_3]$ and $[CO_2]$, as well as measurements of [NO] concentration required for calculation of q are given in [ppmv] (Anderson et al., 1986; Bekker, 2018; Brunelli & Namgaladze, 1988). Other regularities registered make insignificant contribution to the already discovered dependences, so their discussion will not be given.

The performed statistical analysis of T, $[N_2]$, $[O_2]$, $[H_2O]$ and $[O_3]$ has allowed making careful and individual selection of acceptable ranges of heliogeophysical conditions for each

parameter, thus providing for the most correct approach to calculating the profiles of input parameters of the ionization-recombination cycle system within the available data received from satellite.

3.2 Calculation of the ionization rate

As noted above, one of the key parameters of the system of equations (1) is the ionization rate q. The main sources of charged particles at altitudes $h < 100$ km are the cosmic rays (q_{CR}), flux of solar L_α (q_α) and L_β (q_β), flux of hard ultraviolet (q_{UV}) and X-rays emissions (q_{XR}). At increased solar activity, particles falling out of the radiation belts also significantly influence ionization at the polar latitudes (Bekker, 2018; Paulsen et al., 1972; Thomas & Bowman, 1985). In this work, all of the above sources have been taken into account at calculation of the total ionization rate.

It is obvious that the value of q_{XR} actually determines the total ionization rate during the X-ray flare. Satellite data on the radiation flux within three wavelength ranges were used to calculate the q_{XR} during a flare. The measurements in the channels λ_A = 0.05–0.4 nm and λ_B = 0.1–0.8 nm were taken on the GOES satellites (Machol & Viereck, 2016), while the measurements in the channel λ_C = 0.1–7 nm – on the SDO satellite (Woods et al., 2012). The work of Korsunskaya (2019) contains the description of the algorithm of calculating q_{XR} by the solar spectrum from the measurements taken on GOES and SDO satellites.

The ultraviolet part of the spectrum was also calculated on the basis of data obtained from the GOES satellite.

3.3 Calculation of electron concentration

Altitude profiles of electron concentration were calculated for separate VLF paths, for which further verification of the results was carried out. We calculated the profiles along the paths with steps of ~ 300 km that could vary slightly so that the profiles were distributed evenly.

For the simulation we selected several X-ray flares of different classes (C-, M- and X-class), meeting the following conditions:

1. available X-ray solar flux measurements from the GOES and SDO satellites to be used for the ionization rate calculation;

2. full illumination of the European VLF paths during the flares;

3. operable condition of VLF signal transmitters and a receiver located at the Mikhnevo geophysical observatory, allowing verification of the results.

According to these criteria, we selected several X-ray flares of different classes, that occurred in October 2013 and June 2014. Table 2 features the data of the flares under consideration. The data of the quiet days on 22 October 2013 and 8 June 2014 preceding the events listed in Table 2 were used for normalization of the amplitude values.

We selected these two series of consecutive flares of different classes because we also wanted to check if the temporal dynamics of small neutral atmospheric components during the X-radiation growth should be included in the ionospheric models. In our model, the concentrations of small neutrals are considered the external input parameters and are not modified during the

calculation process. If the hard radiation noticeably modifies the small neutrals during a flare, calculation of the sequence of events should give an increasing error for each subsequent flare.

Table 2

Data of the Analyzed Solar Flares

Date	Start time (UT)	Maximum time (UT)	Maximum flux
24 October 2013	09:59	10:09	*M*2.5
24 October 2013	10:30	10:33	*M*3.5
25 October 2013	07:53	08:01	*X*1.7
25 October 2013	09:43	10:12	*M*1.0
9 June 2014	12:24	12:29	*C*9.0
10 June 2014	08:17	08:25	*C*3.9
10 June 2014	09:17	09:31	*C*5.1
10 June 2014	10:04	10:17	*C*5.0
10 June 2014	11:36	11:42	*X*2.2
10 June 2014	12:36	12:52	*X*1.5

Basing on the analysis above, we determined acceptable ranges of heliogeophysical conditions for the selected geographical points and moments of time. The values T, $[N_2]$, $[O_2]$, $[H_2O]$, $[O_3]$ and $[CO_2]$, that fell within the above ranges, were used to construct the probability density functions with an altitude step Δh = 5 km. These functions were used for calculation of the most probable values which we applied to solve the system of differential equations of the ionization-recombination cycle. Ionization rate q was determined as a function of time with step Δt = 1 min. The system of equations (1) was solved for each set of the obtained vertical profiles of input parameters. At the output, we obtained the electron concentrations under calm conditions and during solar flares of different classes.

Figure 4 features the *X*-ray flux registered by GOES satellite, the vertical profile of the ionization rate and electron concentration above the Mikhnevo geophysical observatory during solar flares of *X*- and *M*-classes on 25 October 2013. The electron concentration registered during *X*-ray flares increased by more than 2 orders of magnitude at some altitudes of the *D*-region.

Figure 5 features the *Ne* concentration dynamics at an altitude h = 75 km during the day of 25 October 2013, calculated by using the temperature T and concentration of neutrals M, obtained from the AURA satellite and the MSIS model (Hedin, 1991).

The curves obtained show a difference between the T and M values from MSIS model and the most probable values obtained from satellite. Besides, in Figure 5, one can see a significant contribution to the accuracy of *Ne* concentration calculation, made by not only the ionization rate, but also by temperature and concentration of neutral components. Therefore, we assume that the statistical analysis of the input parameters based on the satellite data should fundamentally improve the *D*-region simulation quality at least for the calm conditions and the *C*- and *M*-class flares when the concentration of *Ne* is the most sensitive to the considered variations.

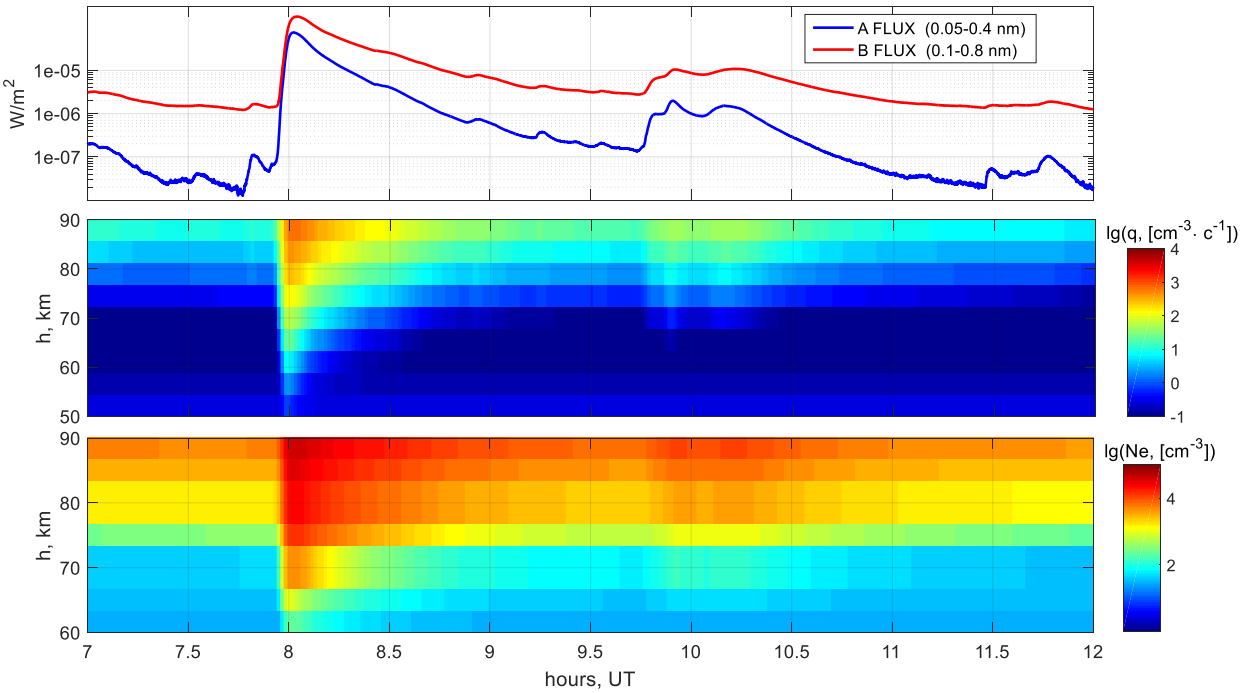

Figure 4. (top panel) *X*-ray flux, (middle panel) ionization rate and (bottom panel) electron concentration during *X*- and *M*-class flares on 25 October 2013 above the Mikhnevo geophysical observatory.

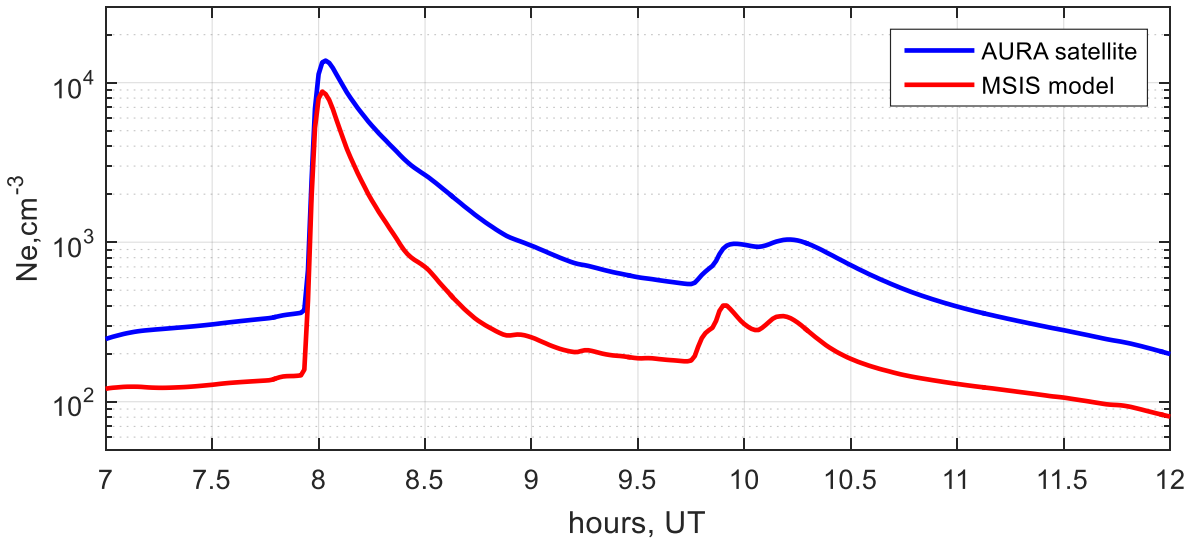

Figure 5. Electron concentration during *X*- and *M*-class flares on 25 October 2013 above the geophysical observatory Mikhnevo, calculated by using the MSIS model and the data received from the AURA satellite.

4 The model verification based on the experimental data on VLF radio wave propagation during *X*-ray flares and discussion of the results

As mentioned above, we used the amplitude characteristics of the VLF transmitter signals (Table 1) received at the Mikhnevo geophysical observatory for verification of the results of modeling the lower ionosphere at the flares listed in Table 2.

Figure 6 presents the results of comparing the obtained theoretical and experimental curves for three flares of different classes that occurred on 25 October 2013 and 9 June 2014. The diagrams show the time variation of the signal from three VLF transmitters - GQD, ICV, FTA.

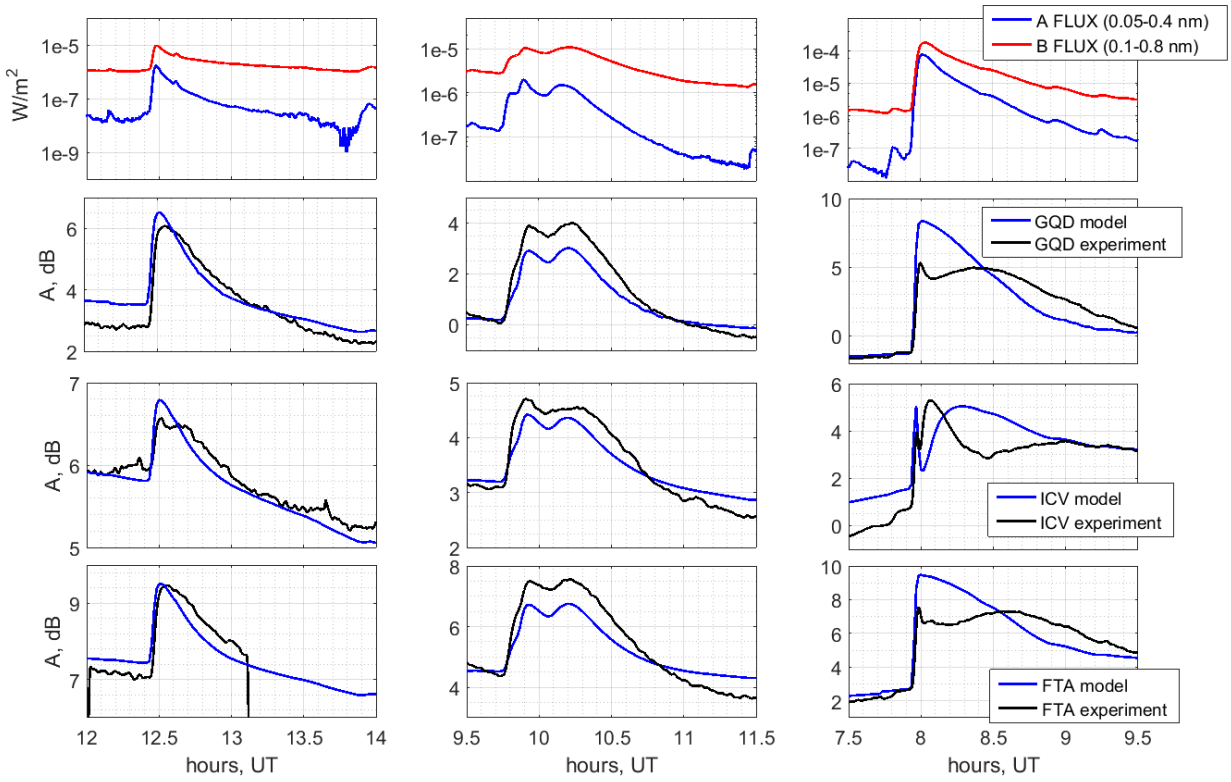

Figure 6. *X*-ray flux from the GOES satellite (top left panel) during the C-class flare on 9 June 2014, (top middle panel) M-class flare on 25 October 2013 and (top right panel) X-class flare on 25 October 2013. Theoretical and experimental time variation of amplitudes of the radio waves (left panels) during the *C*-class flare on 9 June 2014, (middle panels) *M*-class flare on 25 October 2013 and (right panels) *X*-class flare on 25 October 2013, received from the GQD, ICV, FTA transmitters.

It is found out that the constructed plasma-chemical model allows us to predict the amplitude response to the *C*- and *M*-class flares with sufficiently high accuracy, which is evident from the left and middle panels of Figure 6. Moreover, three recurrent flares of *C*-class that occurred on 10 June 2014 are correctly simulated on 5 paths out of 6, which means the low influence of the dynamics of small neutral components.

As for the *M*-class flare, verification of the built lower ionosphere model according to the radiophysical data has showed that the model allows describing not only the qualitative variation of the experimental value of amplitude, but also its quantitative response to the ionization

growth. The difference between the experimental and calculated values is maximum during the highest ionization rate, being within a range of 1dB for all considered paths.

Despite the insignificant difference between the simulated and experimental values, it was not possible to describe the qualitative variation of the signal amplitude in some cases. For example, the theoretical amplitude values for the path ICV–Mikhnevo during the *M*-class flares that occurred on 24 October 2013 keep growing, while the experimental *A* values demonstrate the drastic decrease and vice versa.

The right part of Figure 6 presents the results of simulating the ionospheric response to a *X*-class flare. The amplitude dynamics simulation is not correct in the part following after the flare start at 08:00 UT. Analysis of the Sun's radiation spectrum, based on the RHESSI observatory data has proved presence of ultrahard *X*-radiation in this flare, not described by the current heuristic model of the radiation spectrum and ionization of the lower ionosphere (Korsunskaja, 2019).

A similar result was obtained for the ICV station on 10 June 2014, i.e. the correct modeling of the response to three consecutive flares of *C*-class up to 11:00 UT, and a significant quantitative error at the simulation of two flares of *X*-class at 11:30–14:00 UT (Figure 7).

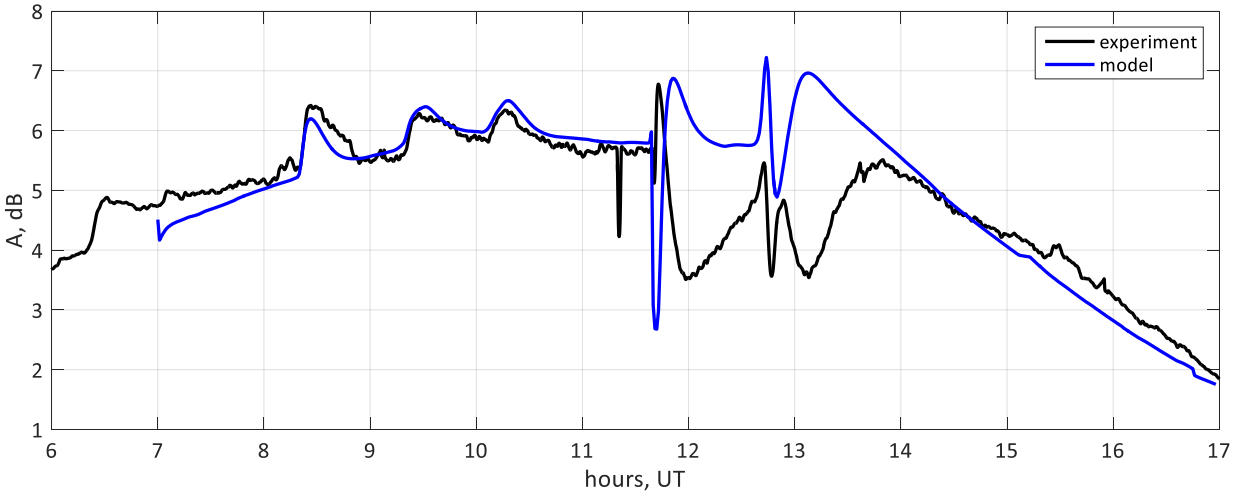

Figure 7. The theoretical and experimental time variation of amplitude of the radio wave due to the *X*-ray flares of *C*- and *X*-class on 10 June 2014, received from the ICV transmitter.

The following work will include further development of the ionization model aimed at the correct account of the ultrahard *X*-radiation, and its advanced verification for all available paths and transmitter frequencies.

In addition to qualitative evaluation of the results obtained, we analyzed the quantitative difference in [dB] between the simulated and experimental values of the radio wave amplitude during the flares considered. For this purpose, a function $D(t) = A_{theor}(t) - A_{exp}(t)$ for 4 days including the days with solar flares listed in Table 2 was analyzed.

As criteria of quality of the obtained results we selected two parameters - the root mean square error (RMSE) and the $D(t)$ module integral rationed by the integration time interval, given in formulas (2), (3):

$$\sigma = \sqrt{\frac{\sum_{i=1}^{n} \left(D_i(t)\right)^2}{n}}; \tag{2}$$

$$I = \frac{\int_{t_1}^{t_2} |D(t)| dt}{t_2 - t_1}. \tag{3}$$

It is obvious that the smaller the values of these parameters, the better the model describes the measured values of the signal amplitude.

Figure 8 shows the obtained values of RMSE and *I* averaged for each class of the flares. On the left, the diagrams are provided with indication of the transmitters from Table 1 and the frequencies at which they operate. Red color shows the lines corresponding to the *X*-class flares, yellow is for *M*-class, green – for *C*-class.

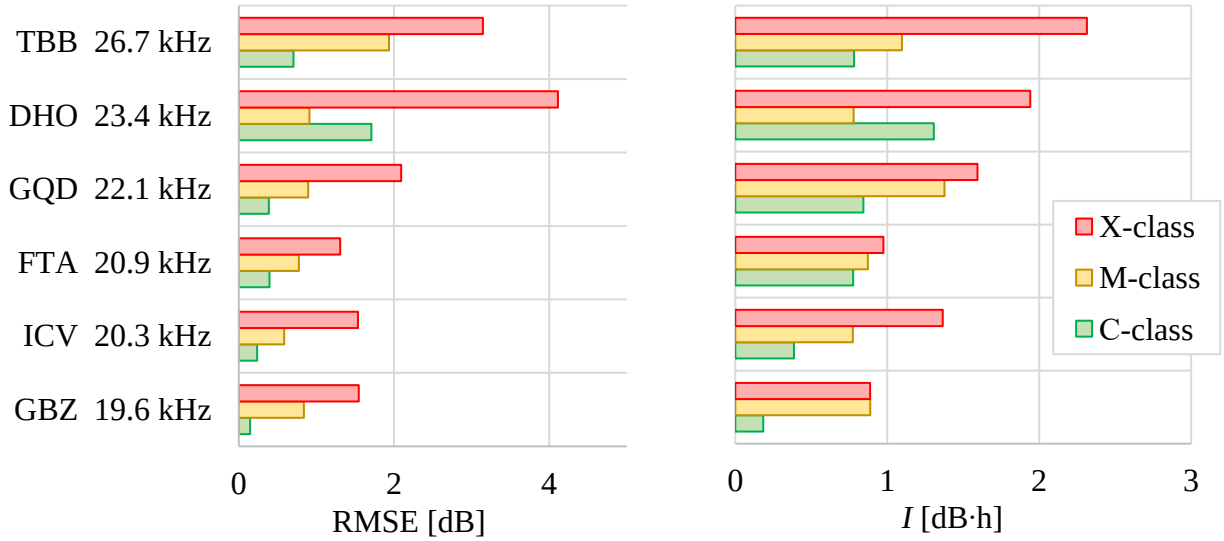

Figure 8. Average values of (left panel) RMSE and (right panel) *I* for six VLF paths.

Additionally, we calculated RMSE and *I* separately for the time intervals corresponding to the ionization growth, i.e. up to the moment when the radiation flux measured on the GOES satellite becomes maximum, and the periods of relaxation after maximums. It is found that the calculated parameters corresponding to the different periods of a flare are almost the same, that is why we do not provide them here.

The obtained criteria provided in Figure 8 confirms the conclusion made at the qualitative evaluation of the theoretical and experimental results agreement; the smaller is the class of simulated flare, the better it is described with use of the constructed model. The only exception is the results obtained for the path DHO–Mikhnevo, i.e. the lowest criteria values correspond to the *M*-class flares on this path.

In addition to the dependence on the flare energy, one can notice some correlation of the results with the transmitter frequency. For example, simulated data for the paths from lower frequency transmitters – GBZ, ICV, FTA, and GQD have a better agreement with the

experimental data for the *X*-class flares. At the same time, there is a significant difference in the path lengths of the transmitters - GBZ, ICV, FTA, GQD and those from DHO and TBB. The two latter show the worse agreement with the experiment. Thus, in terms of modeling high energy flares, the issue of correct calculation of the electron concentration profile defining the geometry of the waveguide remains undecided.

As a result of the verification with use of the data of ground-based radiophysical measurements taken at the Mikhnevo geophysical observatory it is found that the RMSE does not exceed 1 dB for ~80% of cases including *X*-class flares during which the amplitude jump on some paths reaches 8 dB. Qualitative and quantitative analysis of the verification results of the VLF signal amplitude has showed the good predictive capability of the built model for describing weak and moderate ionospheric disturbances.

5 Conclusions

The results of verification of the model simulating the ionospheric *D*-region, performed according to the ground-based radiophysical measurements taken at the Mikhnevo geophysical observatory prove that application of the satellite data of the neutral atmosphere and the ionization rates calculated on the basis of the actual radiation flux values within the *X*-ray and ultraviolet ranges, allows us to describe the lower ionosphere during the *C*- and *M*-class flares with sufficient accuracy. Also, it should be emphasized that a year of high solar activity is characterized by the *C*-class flare level of the background *X*-ray flux. This means that the additional ionization of the lower ionosphere by *X*-ray radiation must be taken into account at any time rather than only at the time of the actual large flare.

When simulating the ionosphere under the condition of the *X*-class flares, we have obtained contradicting results. In our opinion, the main reason for significant errors occurring at *D*-region modeling during the high-level of ionization is the unaccounted ultrahard *X*-radiation. This leads to the inaccurate calculation of the electron concentration profile and, consequently, errors at determining the absolute value of the amplitude response to a sharp growth of ionization. Consequently, this affects the accuracy of describing the environment relaxation after the disturbance. At the same time, we note that the model recovers the background amplitude varying by ~0.5 dB from the experimental value within 1–2 hours after the *X*-class flare event.

Acknowledgments

The study has been conducted with the financial support of the State assignments No. AAAAA 17-117112350014-8 and No. AAAA-A19-1190282790056-6.

The VLF data set used in the present work is collected by the Mikhnevo observatory of Sadovsky Institute of Geospheres Dynamics of Russian Academy of Sciences (http://geospheres-dynamics.com/). The experimental atmospheric data obtained by the AURA satellite are available at https://disc.gsfc.nasa.gov/. The satellite data on the radiation flux obtained by the GOES and SDO satellites are available at http://satdat.ngdc.noaa.gov/sem/goes/data/ and http://lasp.colorado.edu/eve/data_access/evewebdataproducts/. The MSIS model profiles can be obtained under https://ccmc.gsfc.nasa.gov/modelweb/models/msis_vitmo.php. All the other data necessary to reproduce the reported findings are available at https://doi.org/10.5281/zenodo.3779310.

We thank our colleagues from Sadovsky Institute of Geospheres Dynamics, namely, J.A. Korsunskaya for the possibility of use of the ionization model, Yu.V. Poklad and B.G. Gavrilov for the providing radiophysical measurements, S.I. Kozlov and A.N. Lyakhov for the helpful discussions regarding the model constructing and results' verification.

References

Anderson, G. P., Clough, S. A., Kneizys, F. X., Chetwynd, J. H., & Shettle, E. P. (1986). Atmospheric Constituent Profiles (0-120km). *Environmental research papers*. (No. 954). Hanscom, MA: Air Force Geophysics Laboratory.

Bekker, S. Z. (2018). Analysis of electron density calculations using deterministic-probabilistic model of the ionospheric D-region. *Solar-Terrestrial Physics*, 4(3), 67–75. https://doi.org/10.12737/stp-43201809

Bekker, S. Z., Lyakhov, A. N., Kozlov, S. I., & Ryakhovskiy, I. A. (2018). Verification of the deterministic-probabilistic model of the D–region of the ionosphere by the radio physical data obtained in the geophysical observatory Mikhnevo. *Proceedings of SPIE*, 108339P. https://doi.org/10.1117/12.2504295

Bilitza, D., Altadill, D., Truhlik, V., Shubin, V., Galkin, I., Reinisch, B., & Huang, X. (2017). International Reference Ionosphere 2016: from ionospheric climate to real-time weather predictions. *Space Weather*, 15(2), 418–429. https://doi.org/10.1002/2016SW001593

Brunelli, B. E., & Namgaladze, A. A. (1988). *Physics of the ionosphere*. Moscow: Nauka.

Egorova, T., Rozanov, E., Ozolin, Y., Shapiro, A., Calisto, M., Peter, T., & Schmutz, W. (2011). The atmospheric effects of October 2003 solar proton event simulated with the chemistry-climate model SOCOL using complete and parameterized ion chemistry. *Journal of Atmospheric and Solar-Terrestrial Physics*, 73, 356–365. https://doi.org/10.1016/j.jastp.2010.01.009

Egoshin, A. A., Ermak, V. M., Zetzer, Yu. I., Kozlov, S. I., Kudryavtsev, V. P., Lyakhov, A. N., et al. (2012). Influence of meteorological and wave processes on the lower ionosphere during solar minimum conditions according to the data on midlatitude VLF–LF propagation. *Physics of the Solid Earth*, 48(3), 275–286. https://doi.org/10.1134/S1069351312030020

Ferguson, J. A. (1995). Ionospheric model validation at VLF and LF. *Radio Science*, 30(3), 775–782. https://doi.org/10.1029/94RS03190

Ferguson, J. A. (1998). Computer Programs for Assessment of Long-Wavelength Radio Communications, Version 2.0., Technical document 3030. San Diego, CA: Space and Naval Warfare Systems Center.

Friedrich, M., Pock, C., & Torkar, K. (2018). FIRI-2018, an updated empirical model of the lower ionosphere. *Journal of Geophysical Research: Space Physics*, 123, 6737–6751. https://doi.org/10.1029/2018JA025437

Gavrilov, B. G., Ermak, V. M., Poklad, Yu. V., & Ryakhovskii, I. A. (2019a). Estimate of Variations in the Parameters of the Midlatitude Lower Ionosphere Caused by the Solar Flare of September 10, 2017. *Geomagnetism and aeronomy*, 59(5), 587–592. https://doi.org/10.1134/S0016793219050049

Gavrilov, B. G., Zetser, Yu. I., Lyakhov, A. N., Poklad, Yu. V., & Ryakhovskii, I. A. (2017). Spatiotemporal Distributions of the Electron Density in the Ionosphere by Records of the Total Electron Content and Phase of VLF Radio Signals. *Geomagnetism and aeronomy*, 57(4), 461–470. https://doi.org/10.1134/S0016793217040065

Gavrilov, B. G., Zetser, Yu. I., Lyakhov, A. N., Poklad, Yu. V., & Ryakhovskii, I. A. (2019b). Correlated Disturbances of the Upper and Lower Ionosphere from Synchronous Measurements of Parameters of GNSS Signals and VLF Radio Signals. *Cosmic Research*, 57, 36–43. https://doi.org/10.1134/S0010952519010039

Glukhov, V. S., Pasko, V. P., & Inan U. S. (1992). Relaxation of transient lower ionospheric disturbances caused by lightning-whistler-induced electron precipitation bursts. *Journal of Geophysical Research*, 97(A11), 16971–16979. https://doi.org/10.1029/92JA01596

Machol, J., & Viereck, R. (2016). GOES X-ray Sensor (XRS) Measurements. Version 1.4.1. URL: https://www.ngdc.noaa.gov/stp/satellite/goes/doc/GOES_XRS_readme.pdf. NOAA National Centers for Environmental Information (NCEI), University of Colorado, Cooperative Institute for Research in Environmental Science (CIRES), NOAA Space Weather Prediction Center (SWPC).

Grubor, D., Sulic, D., & Zigman, V. (2005). Influence of solar X-ray flares on the earth-ionosphere waveguide. *Serbian Astronomical Journal*, 171, 29–35. https://doi.org/10.2298/SAJ0571029G

Grubor, D., Sulic, D., & Zigman, V. (2008). Classification of X-ray solar flares regarding their effects on the lower ionosphere electron density profile. *Ann. Geophysics*, 26(7), 1731–1740. https://doi.org/10.5194/angeo-26-1731-2008

Han, F., Cummer, S. A., Li, J., & Lu, G. (2011). Daytime ionospheric D region sharpness derived from VLF radio atmospherics. *Journal of Geophysical Research*, 116, A05314. https://doi.org/10.1029/2010JA016299

Hargreaves, J. K. (1995). The solar-terrestrial environment. Cambridge, UK: Cambridge University Press.

Hedin, A. E. (1991). Extension of the MSIS Thermospheric Model into the Middle and Lower Atmosphere. *Journal of Geophysical Research*, 96(A2), 1159–1172. https://doi.org/10.1029/90JA02125.

Korsunskaja, J. A. (2019). Heuristic model of solar x-ray spectrum according to satellite data for geophysical applications. *Solar-Terrestrial Physics*, 5(3), 75–86. https://doi.org/10.12737/stp-53201909

Krivolutsky, A. A., Cherepanova, L. A., V'yushkova, T. Y., & Repnev, A. I. (2015). The three-dimensional global numerical model CHARM-I: The incorporation of processes in the ionospheric D-region. *Geomagnetism and aeronomy*, 55(4), 467–486. https://doi.org/10.1134/S0016793215030123

Kudryavtsev, V.P., Romanyukha, N.Yu. (1995). Modelling of ionization-recombination processes in the middle atmosphere. *Mathematical Modeling*, 7(3), 3–18.

Kumar, A., & Kumar, S. Earth Planets Space (2018). 70: 29. https://doi.org/10.1186/s40623-018-0794-8

Kumar, S., Kumar, A., Menk, F., Maurya, A. K., Singh, R., & Veenadhari, B. (2015). Response of the low-latitude D region ionosphere to extreme space weather event of 14–16 December 2006. *Journal of Geophysical Research: Space Physics*, 120, 788–799. https://doi.org/10.1002/2014JA020751

Kumar, S., NaitAmor, S., Chanrion, O., & Neubert, T. (2017). Perturbations to the lower ionosphere by tropical cyclone Evan in the South Pacific region. *Journal of Geophysical Research: Space Physics*, 122, 8720–8732. https://doi.org/10.1002/2017JA024023

Livesey, N.J., Read, W.G., Lambert, A., Cofield, R.E., Cuddy D.T., Froidevaux L., et al. (2013). Aura Microwave Limb Sounder (MLS). Version 2.2 and 2. URL: https://mls.jpl.nasa.gov/data/v2-2_data_quality_document.pdf. California Institute of Technology, Pasadena, California.

Lyakhov, A. N., Korsunskaya, J. A., Gavrilov, B. G., Ryakhovskiy, I. A., Bisyarin, M. A., Kirillov, V. V., et al. (2018). Verification of the empirical lower ionosphere models on VLF observations at midlatitude Mikhnevo geophysical observatory. *Proceedings of SPIE*, 108339N. https://doi.org/10.1117/12.2504293

Marsh, D. R., Mills, M., Kinnison, D., Lamarque, J.-F., Calvo, N., & Polvani, L. (2013). Climate change from 1850 to 2005 simulated in CESM1 (WACCM). *Journal of Climate*, 26(19), 7372–7391. https://doi.org/10.1175/JCLI-D-12-00558

Maurya, A. K., Veenadhari, B., Singh, R., Kumar, S., Cohen, M. B., Selvakumaran, R., et al. (2012). Nighttime D region electron density measurements from ELF-VLF tweek radio atmospherics recorded at low latitudes. *Journal of Geophysical Research*, 117, A11308. https://doi.org/10.1029/2012JA017876

Maurya, A. K., Venkatesham, K., Kumar, S., Singh, R., Tiwari, P., & Singh, A. K. (2018). Effects of St. Patrick's Day geomagnetic storm of March 2015 and of June 2015 on low-equatorial D region ionosphere. *Journal of Geophysical Research: Space Physics*, 123, 6836–6850. https://doi.org/10.1029/2018JA025536

Mitra, A.P. (1974). *Ionospheric Effects of Solar Flares*. Dordrecht: Reidel.

Nava, B., Coïsson, P., & Radicella, S. M. (2008). A new version of the NeQuick ionosphere electron density model. *Journal of Atmospheric and Solar-Terrestrial Physics*, 70(15), 1856–1862. https://doi.org/10.1016/j.jastp.2008.01.015

Nina, A., Cadez, V., Sulic, D., Sreckovic, V., & Zigman, V. (2011). Effective electron recombination coefficient in ionospheric D-region during the relaxation regime after solar flare from February 18, 2011. *Nuclear Instruments and Methods in Physics Research B*, 279, 106–109. https://doi.org/10.1016/j.nimb.2011.10.026

Palit, S., Basak, T., Mondal, S. K., Pal, S., & Chakrabarti, S. K. (2013). Modelling of the Very Low Frequency (VLF) radio wave signal profile due to solar flares using the GEANT4 Monte Carlo simulation coupled with ionospheric chemistry. *Atmospheric Chemistry and Physics*, 13, 9159–9168. https://doi.org/10.5194/acp-13-9159-2013

Paulsen, D. E., Huffman, R. E., & Larrabe, J. C. (1972). Improved photoionization rates of $O_2(^1\Delta_g)$ in the D – region. *Radio Science*, 7(1), 51–55. https://doi.org/10.1029/RS007i001p00051

Peter, W. B., Chevalier, M. W., & Inan, U. S. (2006). Perturbations of mid-latitude subionospheric VLF signals associated with lower ionospheric disturbances during major geomagnetic storms. *Journal of Geophysical Research*, 111, A03301. https://doi.org/10.1029/2005JA011346

Poppoff, I. G., & Whitten, R. C. (1962). D-Region Ionization by Solar X Rays. *Journal of Geophysical Research*, 67(7), 2986–2988. https://doi.org/10.1029/JZ067i007p02986

Ryakhovskiy, I. A., Gavrilov, B. G., Lyakhov, A. N., Poklad, Y. V., Bekker, S. Z., & Kozlov, S. I. (2018). Ionization of the lower ionosphere during the X-ray solar flare on September 6, 2017. *Proceedings of SPIE*, 108339Y. https://doi.org/10.1117/12.2504402

Schunk, R. W., & Nagy A. (2009). Ionospheres: Physics, Plasma Physics, and Chemistry. Cambridge, UK: Cambridge University Press.

Thomas, L., & Bowman, M. R. (1985). Model studies of the D-region negative-ion composition during day-time and night-time. *Journal of Atmospheric and Solar-Terrestrial Physics*, 47(6), 547–556.

Thomson, N. R., Rodger, C. J., & Clilverd, M. A. (2005). Large solar flares and their ionospheric D region enhancements. *Journal of Geophysical Research*, 110(A9), 6306. https://doi.org/10.1029/2005JA011008

Thomson, N. R., Rodger, C. J., & Dowden, R. L. (2004). Ionosphere gives size of greatest solar flare. *Geophysical Research Letters*, 31, L06803. https://doi.org/10.1029/2003GL019345

Turunen, E., Matveinen H., & Ranta H. (1992). Sodankyla Ion Chemistry (SIC) model. Rept. 49. Finland: Sodankyla Geophysical Observatory.

Turunen, E., Tolvanen, J., Matveinen, H., & Ranta H. (1996). D Region Ion Chemistry Model. *STEP Handbook of Ionospheric Models* (pp. 1–25). Boulder, CO: Utah State University.

Verronen, P. T., Andersson, M. E., Marsh, D. R., Kovacs, T., & Plane, J. M. C. (2016). WACCM-D – Whole atmosphere community climate model with D-region ion chemistry. *Journal of Advances in Modeling Earth Systems*, 8(2), 954–975. https://doi.org/10.1002/2015MS000592

Verronen, P. T., Seppala, A., Clilverd, M. A., Rodger, C. J., Kyrola, E., Enell, C.-F., et al. (2005). Diurnal variation of ozone depletion during the October-November 2003 solar proton events. *Journal of Geophysical Research*, 110, A09S32. https://doi.org/10.1029/2004JA010932

Wait, J. R., & Spies, K. P. (1964). Characteristics of the Earth-ionosphere waveguide for VLF radio waves. NBS Technical Note 300. Washington, US.

Woods, T.N., Eparvier, F.G., Hock, R., Jones, A.R., Woodraska, D., Judge, D., et al. (2012). Extreme Ultraviolet Variability Experiment (EVE) on the Solar Dynamics Observatory (SDO): Overview of science objectives, instrument design, data products, and model developments. *Solar Phys*ics, 275, 115–143. https://doi.org/10.1007/s11207-009-9487-6.